Bulletin of the Seismological Society of America, Vol. 93, No. 6, pp. 2402–2414, December 2003

Ⓔ

Salton Trough Regional Deformation Estimated from Combined Trilateration and Survey-Mode GPS Data

by Greg Anderson,* Duncan C. Agnew, and Hadley O. Johnson†

Abstract The Salton Trough in southeastern California, United States, has one of the highest seismicity and deformation rates in southern California, including 20 earthquakes M 6 or larger since 1892. From 1972 through 1987, the U.S. Geological Survey (USGS) measured a 41-station trilateration network in this region. We remeasured 37 of the USGS baselines using survey-mode Global Positioning System methods from 1995 through 1999. We estimate the Salton Trough deformation field over a nearly 30-year period through combined analysis of baseline length time series from these two datasets. Our primary result is that strain accumulation has been steady over our observation span, at a resolution of about 0.05 μstrain/yr at 95% confidence, with no evidence for significant long-term strain transients despite the occurrence of seven large regional earthquakes during our observation period. Similar to earlier studies, we find that the regional strain field is consistent with 0.5 $\pm$ 0.03 μstrain/yr total engineering shear strain along an axis oriented 311.6° $\pm$ 23° east of north, approximately parallel to the strike of the major regional faults, the San Andreas and San Jacinto (all uncertainties in the text and tables are standard deviations unless otherwise noted). We also find that (1) the shear strain rate near the San Jacinto fault is at least as high as it is near the San Andreas fault, (2) the areal dilatation near the southeastern Salton Sea is significant, and (3) one station near the southeastern Salton Sea moved anomalously during the period 1987.95–1995.11.

Online material: Tables of stations used in this study and of estimated strain fields.

Introduction

The Salton Trough is the landward extension of the Gulf of California, where the Pacific–North America plate boundary comes on land from the south (Fig. 1). About 90% of the roughly 50 mm/yr relative plate motion across the boundary is taken up on the system of large northwest-trending right-lateral strike-slip faults in the region, including the Cerro Prieto and Imperial fault (IF) zones in the south, the Elsinore and San Jacinto fault (SJF) zones to the west, and the San Andreas fault (SAF) zone on the eastern boundary (Bennett *et al.*, 1996); as a result, this region has one of the highest strain rates in the continental United States.

The Salton Trough also has one of the highest seismicity rates in California, including at least 16 $M \geq 6$ events and at least 4 $M \geq 7$ events since 1890 in an area of about 30,000 km^2. In addition, trenching along the Indio segment of the SAF shows evidence of at least four large slip events between A.D. 1000 and 1700, giving an average recurrence time of approximately 220 years (Sieh, 1986). This segment has not ruptured since approximately A.D. 1685, may have since built up a slip deficit of approximately 7–8 m, and, as noted by Bennett *et al.* (1996), is thus potentially capable of a magnitude 7.5 event.

Given the unique geologic setting and high deformation and seismicity rates, the Salton Trough strain field has been the focus of many geodetic studies, including triangulation, trilateration, leveling, and Global Positioning System (GPS) measurements (e.g., King and Savage, 1983; Feigl *et al.*, 1993; Johnson *et al.*, 1994; Savage and Lisowski, 1995; Bennett *et al.*, 1996). In this article, we describe a study of more than 25 years of trilateration and survey-mode GPS measurements of a geodetic network in the central Salton Trough. We find no evidence for long-term strain-rate changes exceeding our resolution of 0.05 μstrain/yr (at 95% confidence) during our observation period. Consistent with earlier results, we also find that the spatial pattern and magnitude of strain in our study area largely match expectations

*Now at U.S. Geological Survey, 525 Wilson Avenue, Pasadena, California 91106.

†Now at The Prediction Company, 236 Montezuma Avenue, Santa Fe, New Mexico 87501.

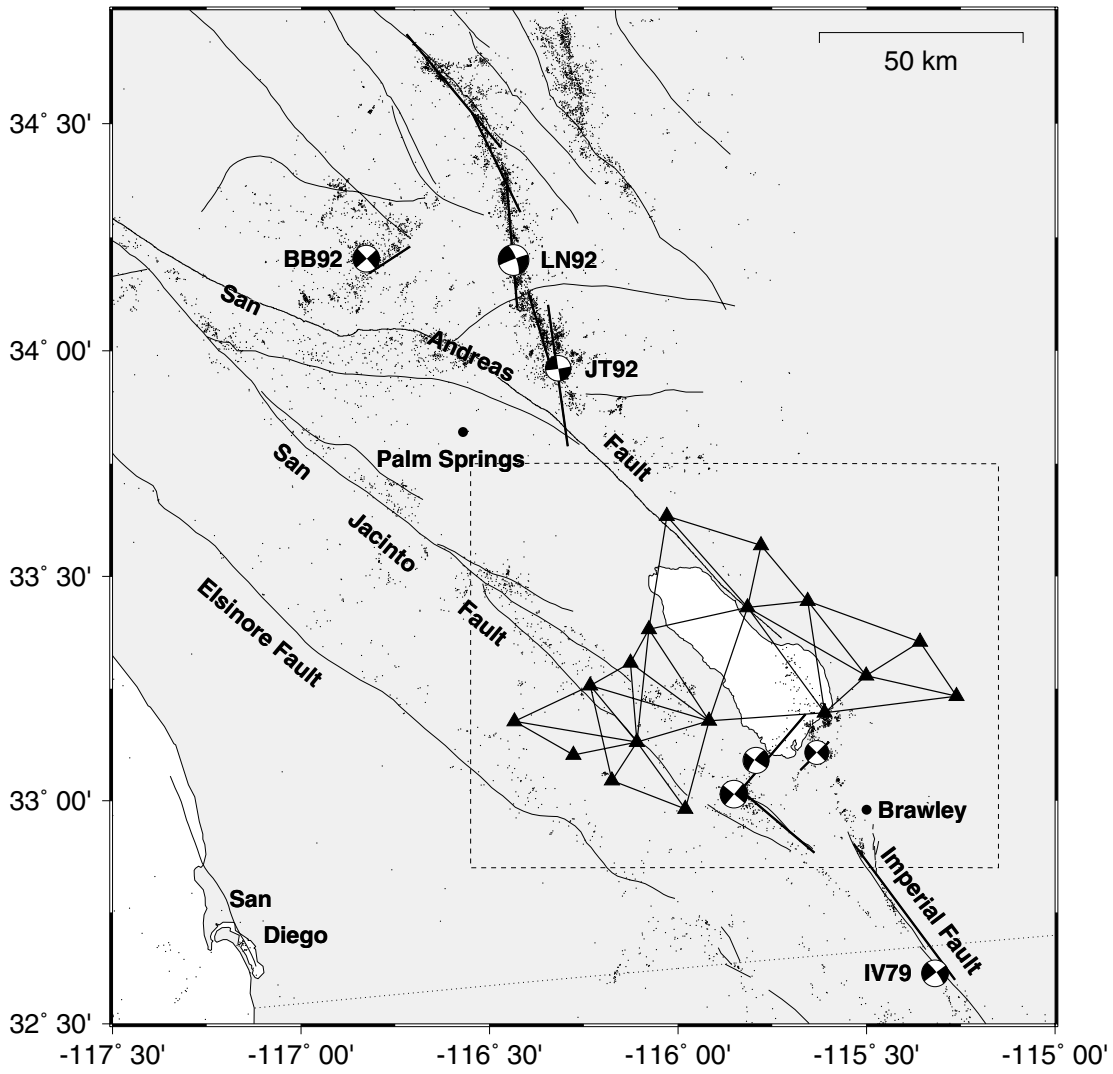

Figure 1. Regional setting of the Salton Trough, California. Light solid lines indicate major regional faults and dots show background seismicity (M >2.5, 1981–2002) from the catalog of Hauksson (2000) and the TriNet catalog. Mainshock focal mechanisms for the M_w 6.6 1979 Imperial Valley (IV79) and M_w 6.1 1992 Joshua Tree (JT92), M_w 7.3 1992 Landers (LN92), and M_w 6.5 1992 Big Bear (BB92) events are shown by the beach balls; heavy lines represent the fault planes used for dislocation modeling of coseismic offsets (see text). The heavy dashed box shows the region used in Figure 2. The dotted line shows the United States–Mexico border, and San Diego, Palm Springs, and Brawley are shown for reference.

from right-lateral strike slip along the SJF and SAF, with the exception of significant regional dilatation near the southeastern Salton Sea.

Data Used

From 1972 through 1987, the U.S. Geological Survey (USGS) made trilateration measurements (Savage and Prescott, 1973) of a 41-station network in the Salton Trough and surrounding mountains (King and Savage, 1983; Johnson *et al.*, 1994; Savage and Lisowski, 1995). They surveyed this network approximately annually, with more frequent observations following significant regional earthquakes. Their final measurements were shortly after the M_w 6.6 24 November 1987 Superstition Hills mainshock.

From 1995 through 1999, we reoccupied 17 of the USGS stations using survey-mode GPS methods; Figure 2 and Table 1 give details on the subnetwork we reoccupied. Figure 3 shows the dates of our surveys and the observation duration on each day, coded by symbols as shown in the lower left corner. We used Trimble 4000 SST antennas and receivers at all stations during the 1995–1998 surveys, except that we used Trimble 4000 SSE equipment at Coach, Mecca, and Orocopia in 1997. We used Ashtech Z-12 receivers with

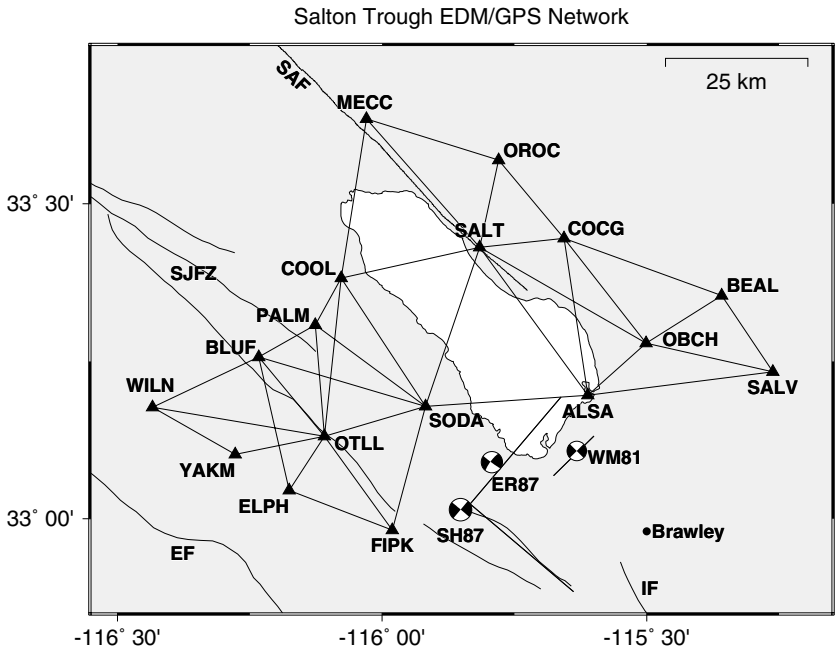

Figure 2. Subset of USGS Salton trilateration network reoccupied using survey-mode GPS. Beach balls indicate the mainshock focal mechanisms for the M_w 5.7 1981 Westmorland (WM81), M_w 6.2 1987 Elmore Ranch (ER87), and M_w 6.6 1987 Superstition Hills (SH87) earthquakes and are plotted at the mainshock epicenters. Thin solid lines show the San Andreas fault (SAF), San Jacinto fault zone (SJFZ), Elsinore fault (EF), and Imperial fault (IF). Heavy solid lines represent the fault planes used for dislocation modeling of coseismic offsets (see text), and Brawley is shown for reference.

Table 1
Salton Network Survey-Mode GPS Stations

Station Code	N. Latitude (°)	E. Longitude (°)	Ellipsoidal Elevation (m)	National Geodetic Survey Permanent Identifier	Stamping
ALSA	33.19636	−115.61117	−73.365	DW1398	ALAMO 1934
ALM3	33.19617	−115.61123	−73.873	–	ALAMO NO 3 1966
ALM4	33.19638	−115.61131	−73.913	–	ALAMO NO 4 1966
ALM5	33.19650	−115.61117	−73.939	–	ALAMO NO 5 1978
BEAL	33.35462	−115.35830	748.051	DW1389	BEALS
BLFA	33.25827	−116.23326	348.790	DX4904	BLUFF 1939 (az. mark)
BLFO	33.25674	−116.23311	359.757	DX4902	Brass rod (Bluff)
COCG	33.44525	−115.65613	659.151	–	COACH 1972
COOL	33.38227	−116.07724	650.012	DX4890	COOLIDGE 1939
ELPH	33.04511	−116.17549	1001.952	–	ELEPHANT 1978
FIPK	32.98178	−115.98077	677.563	DB1601	FISH 1939
MECC	33.63424	−116.02960	467.766	DX4840	MECCA HILL 1931
OBCH	33.27903	−115.50114	−16.025	DW1393	Unstamped disk (Old Beach)
OBC1	33.27925	−115.50123	−16.132	–	OLD BEACH NO 1 1934
OBC2	33.27906	−115.50099	−15.984	–	OLD BEACH NO 2 1934
OBC3	33.28218	−115.49523	−9.994	–	OLD BEACH NO 3 1934
OROC	33.56907	−115.77980	1129.930	DW1485	OROCOPIA 1931
OTLL	33.13119	−116.10905	105.377	DX4908	OCOTILLO 1939 1974
PALM	33.30786	−116.12618	788.851	DX4903	PALM 1939
SALT	33.43096	−115.81564	−3.506	DW1461	SALTON
SALV	33.23365	−115.26148	596.129	DW1379	SALVATION
SD09	33.25686	−116.23317	358.982	–	SDGPS 9 1992
SD91*	33.25700	−116.23305	358.404	–	SDGPS 9 RM1 1992
SOD2	33.17853	−115.91791	30.389	–	SODA NO 2 1939
SODA†	33.17860	−115.91788	31.659	DW1460	Unstamped disk (Soda)
WILN	33.17729	−116.43372	1365.501	DX4934	WILSON 1939
YAKM	33.10238	−116.27750	1081.273	DX4920	YAK 1939

*Station is reset of trilateration mark Bluff RM 1; we use BLUF as the ID for both the trilateration and GPS stations (see Appendix A).
†Station damaged before GPS survey; we made GPS observations at SOD2 and made an eccentric correction to SODA (see Appendix A).
Coordinates in WGS-84. (Table 1 is available online at the SSA Web site.)

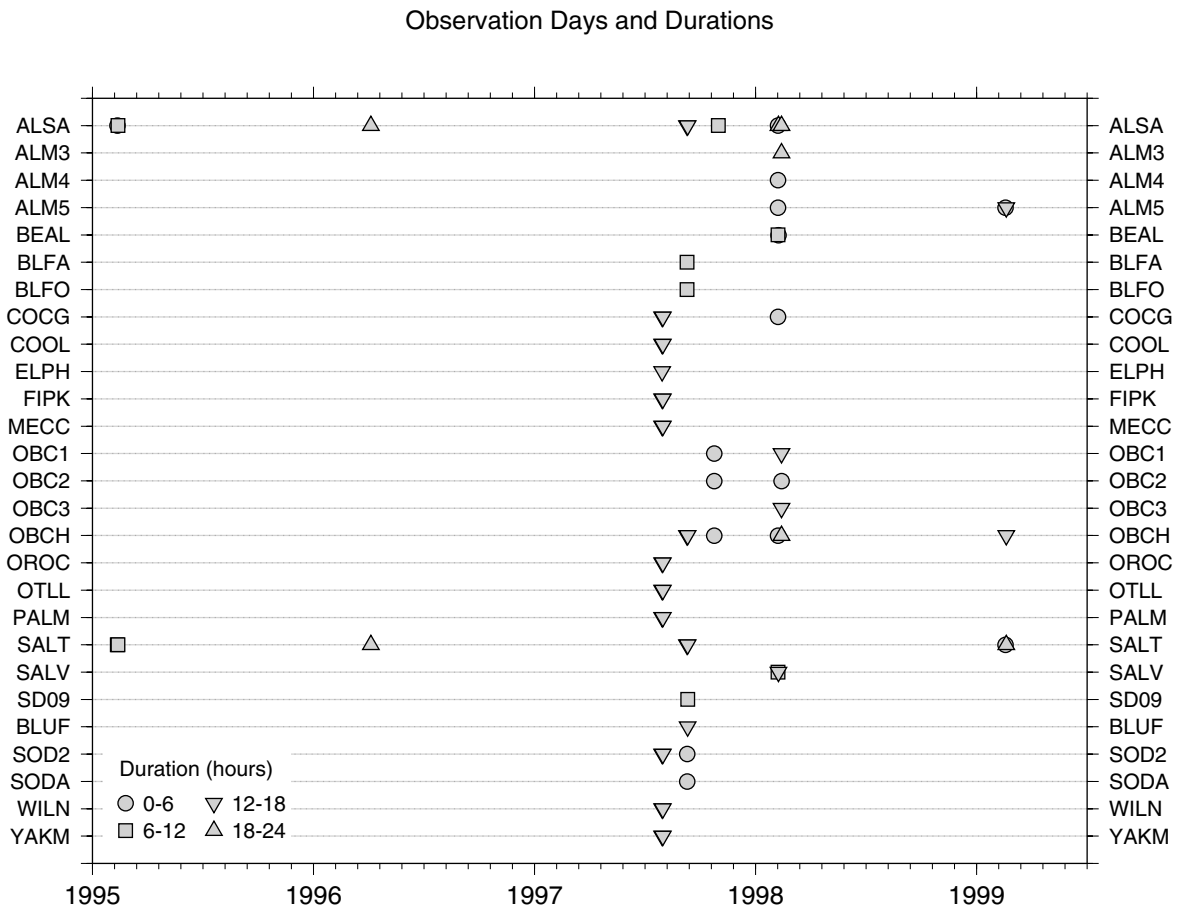

Figure 3. Dates and durations of GPS observations at each station. Circles indicate 0–6 hr observation durations, squares 6–12 hr, inverted triangles 12–18 hr, and triangles 18–24 hr. Observation dates are 1995:041, 1995:042, 1996:095, 1997:211, 1997:211, 1997:252, 1997:253, 1997:297, 1998:037, 1998:038, 1998:043, 1999:048, and 1999:049 (year:day of year).

Dorne–Margolin choke-ring antennas for the 1999 surveys at Salton and Old Beach.

We processed our GPS data using the MIT GAMIT software (King, 1997) to determine baseline lengths and then combined these solutions using GLOBK to estimate baseline length time series. For the GLOBK processing, our survey-mode site coordinates were unconstrained, and we combined these with tightly constrained coordinates for continuous GPS stations Blythe, Durmid Hill, Monument Peak, and Piñon Flat 1 from the Southern California Integrated GPS Network (Hudnut *et al.*, 2002); we did not estimate station velocities, because we combined data from surveys close in time.

Savage and Prescott (1973) described the techniques used in collecting and analyzing, and measurement accuracy of, the trilateration data. They showed that trilateration data errors can be well represented by

$$\sigma^2 = a^2 + b^2L^2, \quad (1)$$

where σ^2 is the variance of the line length, a is a constant term describing the absolute precision of the technique, b is a length-proportional error term, and L is baseline length. Johnson *et al.* (1994) found the best values for a and b in southern California to be 3.8 mm and 0.16 ppm, respectively, and we use these values in our work. For the GPS data, our GAMIT/GLOBK processing returns formal estimates of the uncertainty in baseline length, but these generally underestimate the true variability in the time series, typically by a factor of 2–3 (Anderson, 1999). We thus multiply the GAMIT/GLOBK formal errors by 3 to more accurately reflect the true uncertainty in our GPS data and use those scaled errors in our study.

Time Series Modeling

We combine the GPS and trilateration time series for each baseline (Fig. 4) to determine rates of change for each baseline's length, which we will later convert to baseline strain rate. In doing so, we account for possible systematic length biases between the trilateration and GPS data using the correction of Savage *et al.* (1996). They studied length

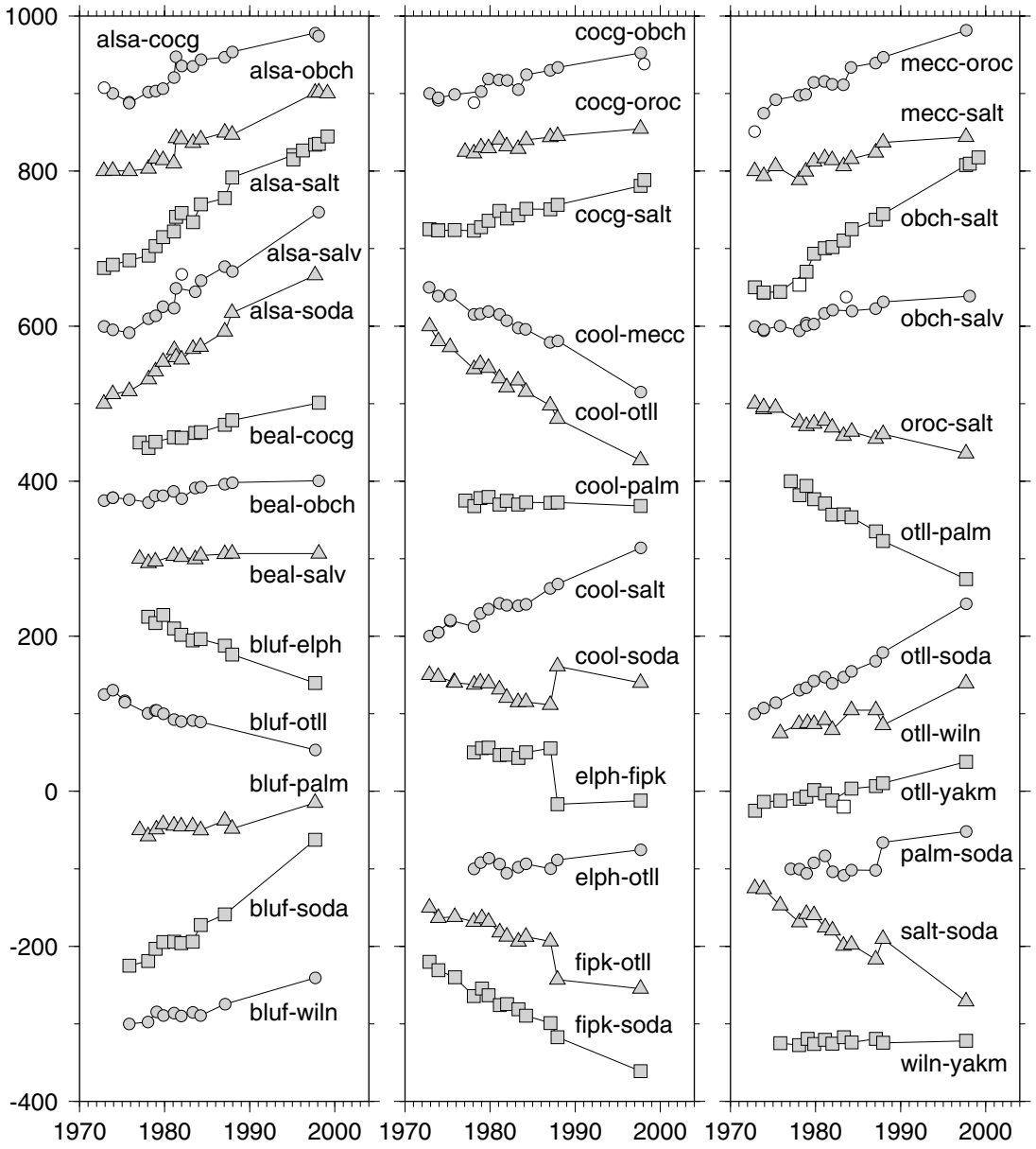

Figure 4. Salton Trough time series. Filled symbols represent data within three standard deviations from model 1 expected data. Open symbols are outliers greater than 3 standard deviations from the model 1 predictions. The vertical scale is in millimeters; time series have been offset arbitrarily for visibility.

estimates from contemporaneous trilateration and GPS observations of 84 baselines in California and found that their trilateration-estimated baseline lengths were systematically 0.283 ± 0.100 ppm longer than their GPS estimates. Accordingly, we shortened the trilateration baseline lengths by 0.283 ppm before combining them with our GPS measurements; the corrections ranged from 2.7 to 9.6 mm for our baseline lengths of 9.4–33.8 km.

To estimate the baseline length change rate for each combined baseline time series, we fit three model types to each series (see Table 2). For model 1, we simultaneously estimate from the data a single rate and coseismic offsets for

Table 2
Model Characteristics

Model	IV79	WM81	ES87	JLB92	1995.0
1	–	Fitted	Fitted	–	Fitted
2	Fitted	Fitted	Fitted	Fitted	–
3	*A priori*	*A priori*	*A priori*	*A priori*	*A priori**

*Model 1 value imposed as *a priori* constraint.

All models have single rate and intercept in addition to specified offsets. 1995.0 offset applies only to ALSA baselines and accounts for anomalous motion of ALSA (see Appendix B). Fitted offsets are estimated from data, *a priori* using dislocation models in Table 3.

the 1981 Westmorland and 1987 Elmore Ranch and Superstition Hills mainshocks (with the latter two being combined into one offset because our temporal resolution does not allow us to treat them independently). For model 2, we simultaneously estimate from the baseline series the same parameters as well as coseismic offsets for the 1979 Imperial Valley earthquake and 1992 Joshua Tree, Landers, and Big Bear events (with the 1992 events again treated as a single offset due to temporal resolution constraints). For model 3, we compute coseismic offsets for all these events from *a priori* mainshock dislocation models (see Table 3), remove these from the data, and then estimate the best-fit single rate. All our models are limited to a single rate for two reasons: (1) our temporal resolution limits our ability to resolve short-term periodic signals, and (2) if we can fit the data with only a single rate, there is no need to invoke long-term rate changes.

Applying these models systematically to all 37 baselines, we find that all but five baselines can be fit adequately at the 95% level by model 1; none of the other models fit all these 32 baselines. Figure 5a shows a typical baseline dataset with the best-fit models shown as lines; residuals for these models are shown in Figure 5b–d. As in all figures, the error bars shown are 95% confidence; all data value uncertainties given in the text and tables are standard deviations. In this case, all sets of residuals are compatible with zero, indicating a good fit, and all three models fit equally well.

None of our models fit at 95% confidence the five remaining baselines, which all involve ALSA and show anomalous deformation that we believe is caused by motion of ALSA between 1987.95 and 1995.11 (Appendix B). We therefore modify model 1 for these five baselines by allowing for an extra offset at 1995.0 to estimate the amount of anomalous motion required. Model 2 cannot be modified to fit the ALSA baselines, as we have insufficient data to constrain both the combined coseismic offset from the 1992 Joshua Tree, Landers, and Big Bear events (JLB92) and 1995.0 offsets. Model 3 requires *a priori* offsets, so we apply the best-fit extra offset from model 1 as an *a priori* constraint. Note that we are not suggesting that all anomalous motion occurred in a single event; by fitting the extra offset, we are only attempting to determine the total amount of anomalous motion, not how or when it occurred. Figure 6 shows the ALSA–OBCH baseline time series and best-fit model 1 as an example of the discrepancies observed in these data.

Model 1 alone fits all baselines at 95% confidence, with the addition of the extra offset for the ALSA baselines. In every case where model 1 and another model fit the data acceptably, using the F test to compare the model fits shows that model 1 is no worse than the other model. Model 1 also has the fewest free parameters, as it only requires two offsets instead of four; we allow only two offsets in this model because the WM81 and ES87 offsets are the only coseismic offsets required by all baselines, and adding more offsets does not improve the fit significantly. We therefore prefer model 1, and the results shown in the rest of this article are generated from model 1.

Results and Discussion

Table 4 shows for each baseline the model 1 best-fit parameters, and Figure 7 shows the strain rates from Table 4 as a map with the network baselines coded by strain rate. We use the baseline strain rates to estimate the horizontal strain-rate tensors for all four-station subnetworks in our network, averaged over the 10- to 30-km width of the subnetworks. We find all baselines observed between the four stations that make up each subnetwork and combine the strain rates for those baselines using the method of Johnson *et al.* (1994) to estimate the average horizontal strain-rate tensor for each subnetwork. We then compute the principal strain rates and axes for each tensor (Ⓔ available as Table 5 online at the SSA web site) and decompose each tensor into the maximum right-lateral engineering shear strain rate ($\dot{\gamma}$, also called the total shear strain rate), azimuth across which the maximum is attained ($\alpha_{\dot{\gamma}}$), and dilatation rate ($\dot{\Delta}$) for each subnetwork (Fig. 8). (Ⓔ Dilatation and shear strain rates available in Table 6 online at the SSA web site.)

Our principal conclusion is that strain accumulation rates in the Salton Trough are very stable over time; we base this on two primary observations. First, all our baseline time

Table 3
Significant Regional Earthquakes, 1972–1999

Date	Name	M_w	N. Latitude (°)	E. Longitude (°)	Code	Model Source
15 October 1979	Imperial Valley	6.6	32.61	−115.32	IV79	Hartzell and Heaton (1983)
26 April 1981	Westmorland	5.7	33.11	−115.63	WM81	Savage and Lisowski (1995)
24 November 1987	Elmore Ranch	6.2	39.09	−115.79	ER87	Larsen *et al.* (1992)
24 November 1987	Superstition Hills	6.6	33.01	−115.85	SH87	Larsen *et al.* (1992)
23 April 1992	Joshua Tree	6.1	33.96	−116.32	JT92	Bennett *et al.* (1995)
28 June 1992	Landers	7.3	34.20	−116.44	LN92	Wald and Heaton (1994)
28 June 1992	Big Bear	6.5	34.20	−116.83	BB92	Wald and Heaton (1994)

We combine the ER87 and SH87 offsets into one offset (ES87) and JT92, LN92, and BB92 into one offset (JLB92) because our temporal sampling does not allow us to resolve individual offsets.

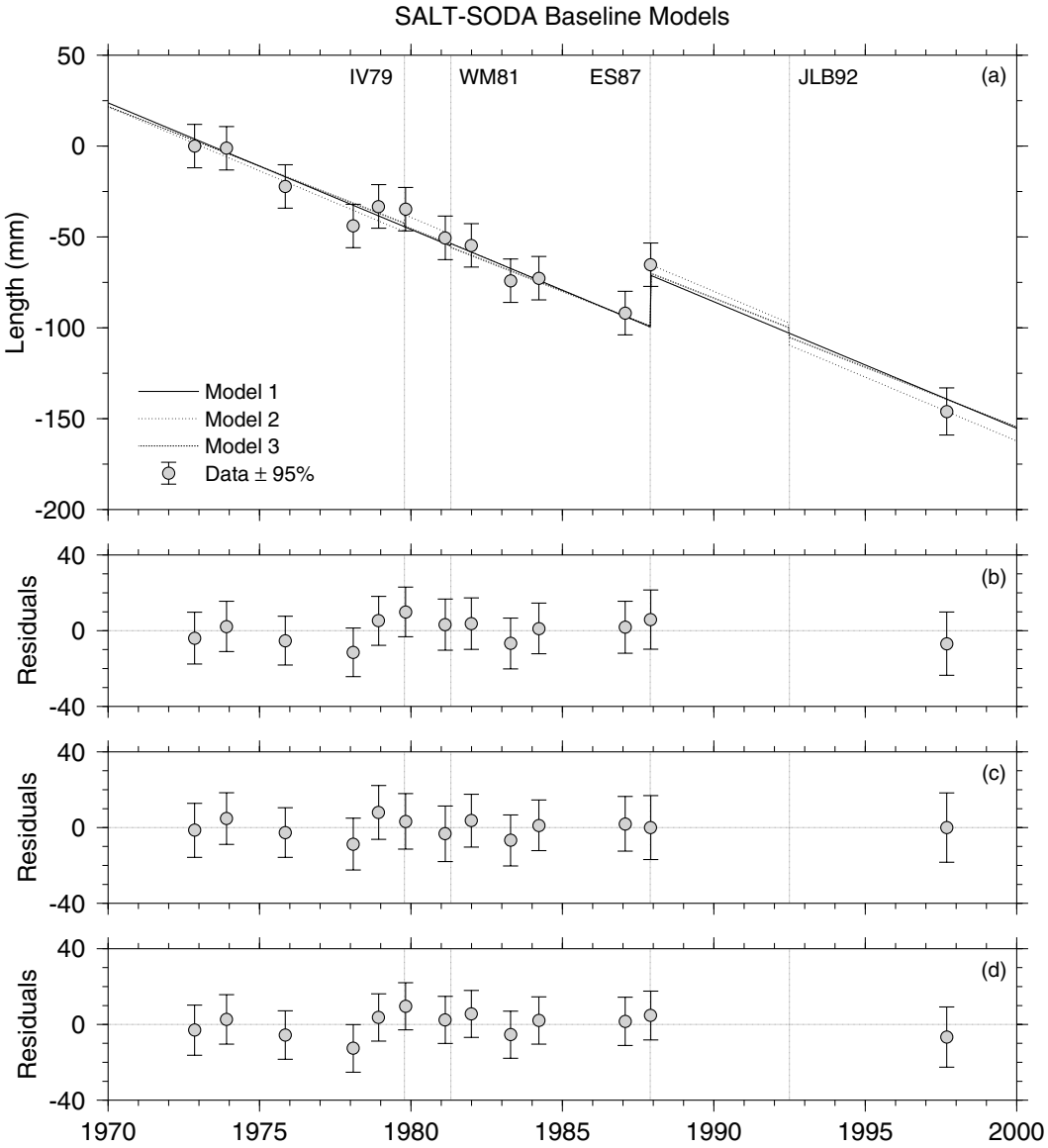

Figure 5. (a) Length time series and model 1–3 fits for SALT–SODA baseline. Data are shown as filled circles with 95% confidence regions. Model 1, 2, and 3 fits are shown by the solid, dotted, and dashed lines, respectively. Note that all models fit the data well and that the rates and offsets fit are approximately similar across all models. Times of the 1979 Imperial Valley (IV79), 1981 Westmorland (WM81), combined 1987 Elmore Ranch and Superstition Hills (ES87), and combined 1992 Joshua Tree, Landers, and Big Bear (JLB92) coseismic offsets are marked by the vertical dotted lines. (b–d) Residuals (in millimeters) for models 1–3, shown as filled circles with 95% confidence regions; note that all residuals are compatible with zero misfit.

series can be fit well by a model with linear strain accumulation in time punctuated by coseismic offsets. Any temporal strain transients must therefore be below our strain-rate uncertainties, and a good upper bound is given by our median 95% uncertainty of 0.046 μstrain/yr. Second, our median $\dot{\gamma}$ for the Salton network as a whole (0.48 $\pm$ 0.15 μstrain/yr along an azimuth of 311.6° $\pm$ 23° east of north) is consistent with the average $\dot{\gamma}$ of 0.35 μstrain/yr along a 319° azimuth found by Johnson *et al.* (1994). Our compatibility with previous analyses, even though we now span roughly twice as much time, argues for consistent strain accumulation in the Salton Trough. Further support for constant strain accumulation comes from the work of Savage (1995), who used principal component analysis to decompose the trilateration data and found that the Salton network data were well explained by steady, linear strain accumulation. While we cannot rule out the possibility of strain transients with either much shorter (such as the groundwater-

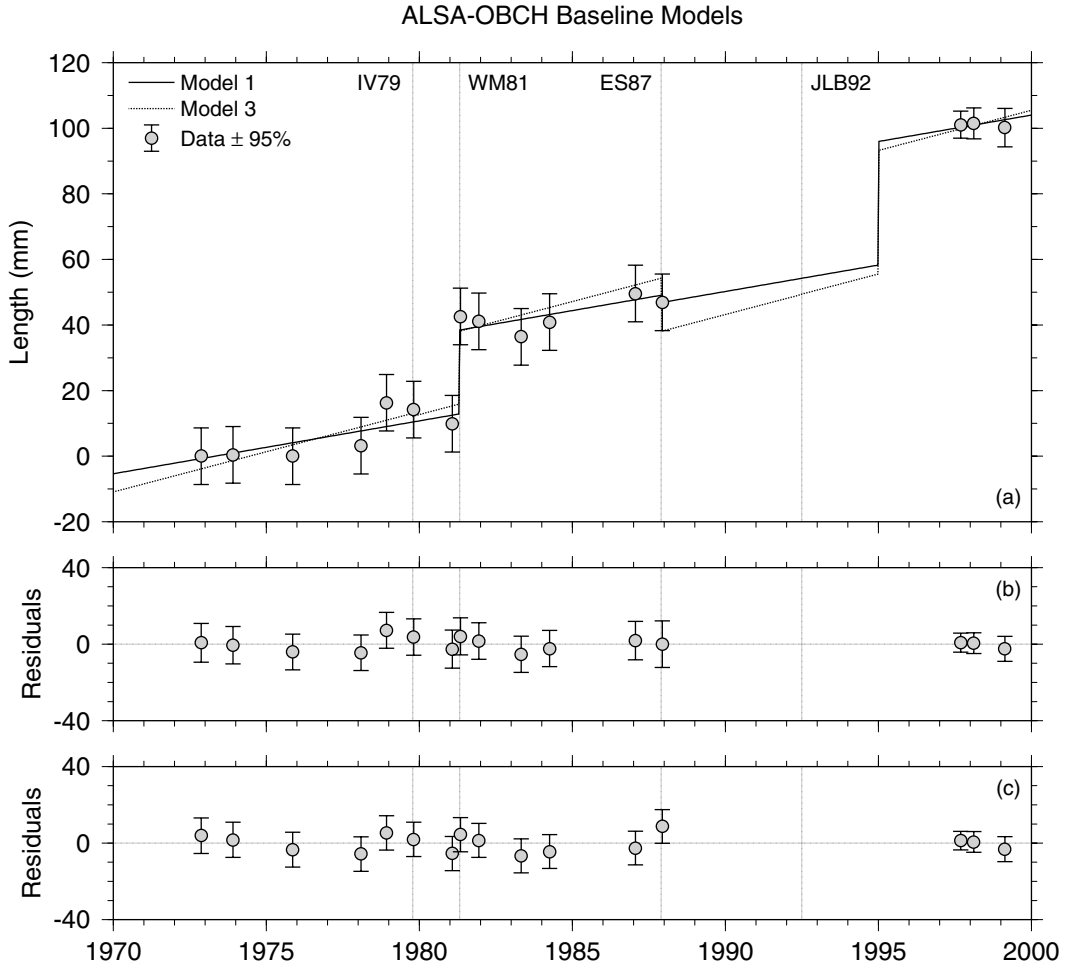

Figure 6. (a) Length time series and model fits for ALSA–OBCH baseline. Lines and circles are as in Figure 5. Note the additional offset at 1995.0 to account for anomalous motion of ALSA; in this case, the discrepancy between the expected value from trilateration and observed GPS measurement is 37.7 ± 6.8 mm. Note that, with the addition of this offset, model 1 fits the data well, while model 3 does not. (b–c) Residuals (in millimeters) for models 1 and 3, as in Figure 5. Note that all residuals are compatible with zero misfit once the additional offset is added.

related signals seen by Bawden *et al.* [2001]) or much longer periods (e.g., very long term postseismic deformation), our results indicate that during our observation span, any fluctuations in strain accumulation rate for the Salton Trough must be less than about 50 nanostrain/yr over periods from about a year to a few decades.

We also find that overall, the Salton Trough strain field is consistent with expectations in a region of primarily northwest–southeast–trending right-lateral strike-slip faults: baselines oriented north–south show compression, and east–west baselines show extension (Fig. 7). Those baselines farthest from the major faults show the least strain; BEAL–SALV, COOL–PALM, ELPH–FIPK, and WILN–YAKM all show insignificant strain rates. Figure 8a shows, for each subnetwork, $\dot{\gamma}$ and $\alpha_{\dot{\gamma}}$ as bars oriented parallel to $\alpha_{\dot{\gamma}}$ and scaled by $\dot{\gamma}$ as shown in the upper left; $\dot{\gamma}$ and $\alpha_{\dot{\gamma}}$ are coherent from one subnetwork to the next, showing the redundancy in the network and indicating coherency in the regional strain field itself. Also, $\alpha_{\dot{\gamma}}$ in any given area is nearly parallel to the strike of the nearest major fault, as appropriate, and rotates smoothly from one orientation to the next. Finally, the median $\dot{\Delta}$ for the network as a whole is insignificant at 0.07 ± 0.08 μstrain/yr, with scattered subnetworks showing significant $\dot{\Delta}$; most of these subnetworks involve the station SODA, perhaps indicating inaccuracies in our corrections for damage to that station (Appendix A).

There are two main departures from this expected picture, both of which have been observed by previous workers. As shown in Figure 8b,d, and as discussed in Johnson *et al.* (1994), the region near the southeastern Salton Sea is undergoing areal dilatation, at a median rate (across the five southeasternmost subnetworks) of 0.18 ± 0.04 μstrain/yr. Johnson *et al.* (1994) suggested two main models to explain this dilatation: an oblique spreading center beneath the

Table 4
Model 1 Baseline Results

Site 1	Site 2	Rate* (mm/yr)	WM81† (mm)	ES87‡ (mm)	1995.0§ (mm)	Strain Rate‖ (10^{-8}/yr)
ALSA	COCG	2.5 ± 0.8	25.6 ± 5.7	1.1 ± 7.3	−1.4 ± 9.8	8.9 ± 2.8
ALSA	OBCH	1.6 ± 0.5	25.6 ± 4.0	−2.2 ± 5.3	37.7 ± 6.8	11.7 ± 3.6
ALSA	SALT	5.7 ± 0.6	16.8 ± 5.4	18.7 ± 7.5	−13.0 ± 8.6	17.5 ± 1.8
ALSA	SALV	4.1 ± 0.8	21.1 ± 6.6	−2.3 ± 7.9	35.1 ± 11.0	12.4 ± 2.3
ALSA	SODA	7.3 ± 0.7	−7.9 ± 5.6	14.6 ± 7.2	−22.9 ± 10.6	25.5 ± 2.3
BEAL	COCG	2.4 ± 0.7	0.4 ± 5.7	5.1 ± 8.2	–	8.1 ± 2.3
BEAL	OBCH	1.0 ± 0.5	2.8 ± 4.3	3.4 ± 5.4	–	6.4 ± 2.9
BEAL	SALV	0.4 ± 0.6	2.0 ± 4.6	0.5 ± 6.2	–	2.6 ± 3.7
BLUF	ELPH	−3.6 ± 0.6	−8.1 ± 4.6	−6.6 ± 7.4	–	−14.8 ± 2.3
BLUF	OTLL	−4.0 ± 0.6	4.4 ± 4.7	21.5 ± 9.4	–	−22.1 ± 3.2
BLUF	PALM	3.0 ± 0.5	−11.4 ± 3.6	−12.7 ± 5.6	–	26.5 ± 3.9
BLUF	SODA	7.2 ± 1.1	−12.0 ± 7.4	20.1 ± 16.8	–	23.5 ± 3.7
BLUF	WILN	2.9 ± 0.9	−8.8 ± 6.0	4.5 ± 13.0	–	14.1 ± 4.4
COCG	OBCH	2.4 ± 0.4	−2.7 ± 4.6	1.2 ± 6.1	–	10.4 ± 1.8
COCG	OROC	1.5 ± 0.5	−1.1 ± 4.0	−0.7 ± 6.4	–	8.2 ± 2.6
COCG	SALT	2.5 ± 0.4	−0.9 ± 3.8	2.8 ± 5.2	–	16.4 ± 2.4
COOL	MECC	−5.7 ± 0.5	7.4 ± 4.9	−0.5 ± 6.8	–	−20.3 ± 1.7
COOL	OTLL	−6.2 ± 0.5	−1.7 ± 4.9	−5.8 ± 6.8	–	−22.2 ± 1.7
COOL	PALM	−0.4 ± 0.4	0.3 ± 3.5	1.3 ± 5.5	–	−4.1 ± 4.5
COOL	SALT	4.6 ± 0.4	−8.2 ± 4.6	5.2 ± 6.2	–	18.6 ± 1.7
COOL	SODA	−1.9 ± 0.6	−11.7 ± 5.2	51.8 ± 6.8	–	−7.1 ± 2.0
ELPH	FIPK	0.6 ± 0.5	−6.1 ± 4.1	−69.2 ± 6.7	–	3.2 ± 2.5
ELPH	OTLL	1.3 ± 0.5	−12.2 ± 3.6	6.2 ± 5.7	–	11.3 ± 3.9
FIPK	OTLL	−1.7 ± 0.4	−13.4 ± 4.2	−41.7 ± 5.8	–	−8.4 ± 2.0
FIPK	SODA	−5.5 ± 0.5	1.9 ± 4.8	−6.9 ± 6.1	–	−24.4 ± 2.2
MECC	OROC	4.3 ± 0.5	−1.8 ± 4.5	0.2 ± 6.6	–	17.7 ± 1.9
MECC	SALT	1.2 ± 0.5	4.0 ± 5.2	13.1 ± 7.1	–	4.1 ± 1.6
OBCH	SALT	6.7 ± 0.5	4.5 ± 5.6	−1.7 ± 7.5	–	19.9 ± 1.4
OBCH	SALV	1.1 ± 0.5	11.6 ± 4.9	4.2 ± 6.2	–	5.0 ± 2.0
OROC	SALT	−2.9 ± 0.4	−2.2 ± 3.9	12.8 ± 5.3	–	−18.5 ± 2.3
OTLL	PALM	−5.1 ± 0.5	−7.9 ± 4.1	−8.0 ± 6.6	–	−26.0 ± 2.5
OTLL	SODA	6.0 ± 0.5	−14.4 ± 4.4	6.3 ± 5.7	–	32.0 ± 2.4
OTLL	WILN	5.1 ± 0.6	−18.3 ± 5.6	−24.8 ± 8.2	–	16.6 ± 1.9
OTLL	YAKM	2.8 ± 0.4	−10.6 ± 4.2	1.9 ± 5.5	–	17.1 ± 2.4
PALM	SODA	1.7 ± 0.7	−16.4 ± 5.0	30.5 ± 7.2	–	7.1 ± 2.8
SALT	SODA	−7.0 ± 0.6	1.4 ± 5.5	28.4 ± 7.2	–	−23.5 ± 1.9
WILN	YAKM	0.4 ± 0.5	0.1 ± 4.0	−5.6 ± 6.2	–	2.4 ± 2.7

*Rate of change of baseline length.
†1981 Westmorland earthquake coseismic offset.
‡1987 Elmore Ranch/Superstition Hills combined coseismic offset.
§Additional offset for ALSA discrepancy.
‖Baseline linear strain rate, extension positive.
Positive rates and offsets indicate that a particular baseline is lengthening. For ALSA baselines, a positive offset indicates ALSA moved away from the other station. (Ⓔ Table 4 is available online at the SSA website.)

Brawley Seismic Zone and a leaky transform connecting the IF and SAF through the Brawley Seismic Zone. While neither model adequately explained all the trilateration data, Johnson *et al.* (1994) preferred the oblique spreading center model.

Consistent with studies by Johnson *et al.* (1994) and Bennett *et al.* (1996), we also find that $\dot{\gamma}$ is higher near the SJF than near the SAF; this is most easily seen as the decrease from southwest (near the SJF) to northeast (near the SAF) in the network-crossing profile of $\dot{\gamma}$ shown in Figure 8c. This strain gradient could be caused by a number of effects. First, the subnetworks near the SAF are generally larger, which might bias the average rates to lower values; however, Johnson *et al.* (1994) showed that the network geometry alone could not be responsible. Also, perhaps there is ongoing postseismic relaxation after the 1968 *M* 6.5 Borrego Mountain earthquake, which occurred close to the west side of the Salton network. We discount this possibility since no baselines show anything but steady strain accumulation and because no earthquakes in the Salton Trough during our observation span exhibit significant postseismic transients.

If strain in the Salton Trough is primarily caused by steady slip along the SJF and SAF below some depth (the locking depth), the higher rates near the SJF imply either a

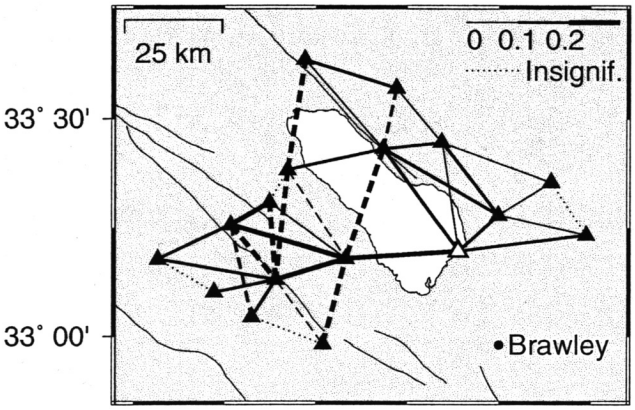

Figure 7. Baseline strain rates for model 1. Baselines that are stretching are solid, while contracting lines are dashed; line thickness varies with strain rate as shown in upper right, with values in microstrain per year. ALSA is marked by an empty triangle to emphasize that the ALSA baselines have an additional offset. Dotted lines represent baselines with insignificant (at 95% confidence) strain rates. Note expected pattern of north–south compression and east–west extension.

shallower locking depth or a higher rate of slip for the SJF compared with the SAF. A commonly used proxy for the locking depth is the depth of seismicity. In the polygon bounded by BLUF, PALM, COOL, SODA, FIPK, ELPH, and YAKM, 90% of the approximately 5000 earthquakes relocated by Richards-Dinger and Shearer (2000) occurred at depths shallower than 12 km. There are many fewer earthquakes along the southern SAF, so to define this seismicity we used a polygon consisting of OROC, COCG, a point 10 km southwest of SALT, and a point 10 km west of MECC, which excludes the northernmost Brawley Seismic Zone. There are only 220 earthquakes in the catalog inside this region, and 90% of them are shallower than 8 km, implying a shallower locking depth on the SAF.

We therefore believe that the higher strain rate is caused by a higher slip rate at depth along the SJF than along the SAF; this conclusion is somewhat controversial, but it is supported by additional evidence. First, Johnson (1993) used extremal methods to invert trilateration data spanning the Elsinore fault, SJF, and SAF for self-consistent bounds on slip rates along those faults and showed that the SJF and SAF slip rate bounds were 7–25 and 11–23 mm/yr, respectively, allowing a faster SJF slip rate. It is important to note, however, that the block model analysis by Bennett *et al.* (1996) of survey-mode GPS data in this region gives slip rates of 26 ± 2 and 9 ± 2 mm/yr on the SAF and SJF, respectively. Recent geologic work also supports comparable or higher slip rates along the SJF relative to the SAF. Rockwell *et al.* (1990) found a slip rate of 6–23 mm/yr (preferred range: 12–13 mm/yr) along the Anza segment of the SJF, while work by Brown (1990) gave an estimate of 10–17 mm/yr, and Kendrick *et al.* (2002) argued for ≥20 mm/yr along the northern SJF. Dorsey (2003) has improved the Keller *et al.* (1982) alluvial fan offset measurements and gave a new SAF slip rate estimate of 15 ± 3 mm/yr, which is in good agreement with the 6–12 mm/yr rate determined by Sieh and Williams (1990) near Salt Creek. A reasonable range of geologic slip rate estimates is thus 15–20 mm/yr for the SJF and about 15 mm/yr for the SAF, and the Johnson (1993) work allows for a faster SJF, so it is at least plausible that the current slip rate at depth along the SJF is comparable to or faster than that along the SAF. A more definitive result may be possible from a future analysis of all the data (trilateration and independent GPS) collected in this region, which is in the process of being assembled by the Southern California Earthquake Center.

Conclusions

We have combined trilateration and survey-mode GPS observations of a 17-station network in the Salton Trough to study deformation of that region. We find that our data are fit well by linear strain accumulation, punctuated by coseismic offsets at the times of the 1981 Westmorland and 1987 Elmore Ranch and Superstition Hills mainshocks. There is no evidence for significant long-term strain transients at a resolution of about 0.05 μstrain/yr, even though seven significant regional earthquakes occurred during our observation span. The overall strain field is well represented by about 0.5 ± 0.03 μstrain/yr of total engineering shear strain along an orientation 311.6° ± 23° east of north, approximately parallel to the strike of the SAF and SJF, the major faults crossed by our network.

We also find that the shear strain rate near the SJF is at least as high as that along the SAF, which we believe is caused by a higher slip rate at depth along the SJF. Perhaps due to a spreading center or leaky transform fault beneath the Brawley Seismic Zone, we find 0.18 ± 0.04 μstrain/yr of areal dilatation near the southeastern Salton Sea. Finally, ALSA, a station located near the southeastern Salton Sea, moved anomalously 35.6 ± 8.1 mm to the west-southwest during the period 1987.95–1995.11, most likely in response to nearby geothermal power production.

Acknowledgments

Our fieldwork would have been impossible without the efforts and skill of Wade Blackard, Steve Bralla, Stephen Dockter, and Don Elliott, and we thank them for their help. We thank Landells Aviation, in particular our pilot Steve, for flying us to mountaintop survey points that would have been difficult if not impossible to reach otherwise (including some we would have bet you could not land on). Master Chief Horner with Naval Special Weapons Group 1 and Gunnery Sergeant Andrew Fenwick at Marine Corps Air Station Yuma were very helpful in arranging access to sites Coach, Beals, and Salvation, which are located in the Chocolate Mountains Aerial Gunnery Range. We used trilateration data collected by the USGS Crustal Strain Group, and we thank them for their efforts and for making the data available to us. We acknowledge the Southern California Integrated GPS Network and its sponsors, the W. M. Keck Foundation, NASA, NSF,

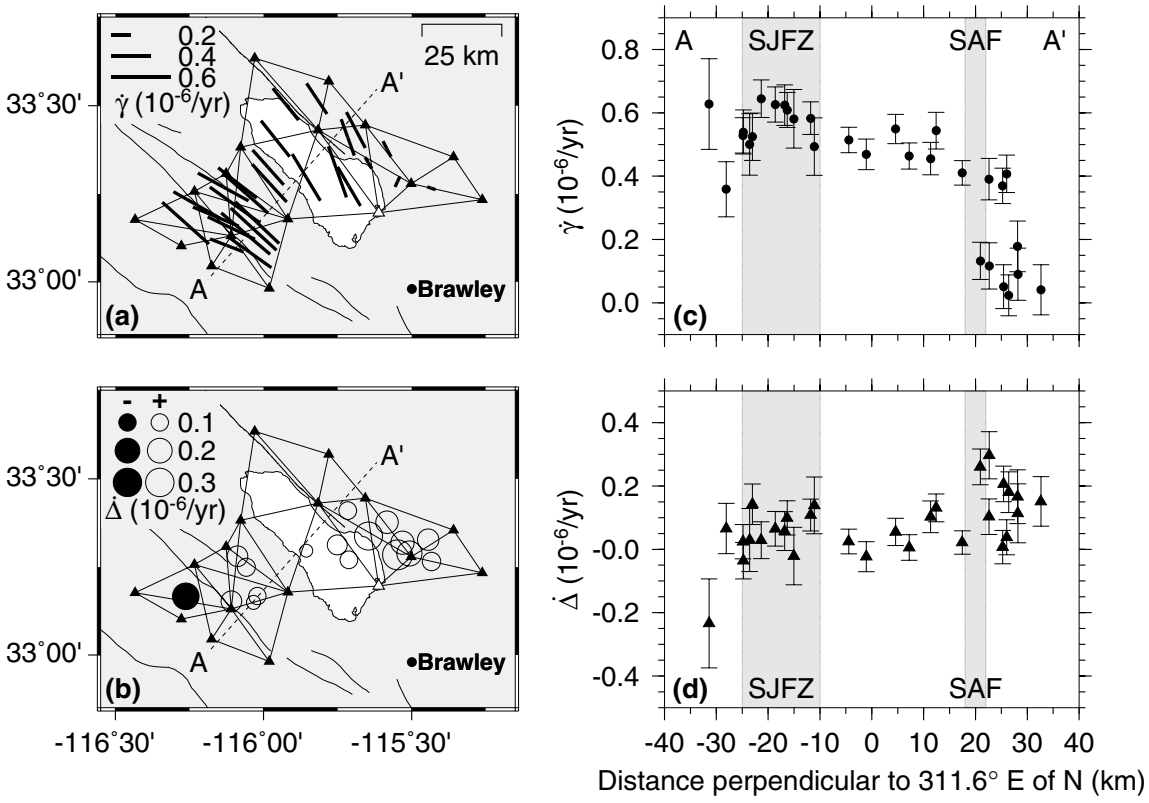

Figure 8. (a) $\dot{\gamma}$ and $\alpha_{\dot{\gamma}}$ for each unique four-station subnetwork, using the model 1 principal strain rates. Bars are plotted at the centroid of each subnetwork with significant $\dot{\gamma}$, scale with $\dot{\gamma}$ as shown in the upper left, and are oriented parallel to $\alpha_{\dot{\gamma}}$. (b) $\dot{\Delta}$ for only those subnetworks with significant $\dot{\Delta}$. Open circles, $\dot{\Delta} > 0$; solid circles, $\dot{\Delta} < 0$. Circles scale with $\dot{\Delta}$ as shown in upper left. (c) Cross-network profile of $\dot{\gamma}$ (with 95% confidence regions) along the line AA′ in (a). Bands labeled "SJFZ" and "SAF" refer to the San Jacinto fault zone and San Andreas fault, respectively. The SJFZ band is wider because the SJFZ has multiple fault strands through our network, while the SAF is relatively simple. (d) Profile of dilatation rates. Note high $\dot{\Delta}$ in southeastern part of network.

USGS, and SCEC, for providing data used in this study. We created our figures using the Generic Mapping Tools (Wessel and Smith, 1991, 1998) and we thank Pål Wessel, Walter Smith, and all the others who have contributed to that software suite. This work makes use of event locations computed using waveforms recorded by the Southern California Seismic Network (SCSN), which is operated jointly by the Seismological Laboratory at Caltech and the U.S. Geological Survey, Pasadena. We thank Ken Hudnut and Nancy King for thoughtful reviews of this manuscript and many fruitful discussions of the work in progress. This research was supported by NSF Grant EAR-96286744 and U.S. Geological Survey NEHRP Grant 1434-HQ-97-GR-02979. This research was supported by the Southern California Earthquake Center. SCEC is funded by NSF Cooperative Agreement EAR-0106924 and USGS Cooperative Agreement 02HQAG0008. The SCEC Contribution Number for this paper is 730.

References

Anderson, G. J. (1999). I. Studies in crustal deformation using GPS and tiltmeters; II. New statistical techniques in static stress triggering. *Ph.D. Thesis*, University of California, San Diego, La Jolla, California.

Bawden, G. W., W. Thatcher, R. S. Stein, K. W. Hudnut, and G. Peltzer (2001). Tectonic contraction across Los Angeles after removal of groundwater pumping effects, *Nature* **412,** 812–815.

Bennett, R. A., R. E. Reilinger, W. Rodi, Y. Li, and M. N. Toksöz (1995). Coseismic fault slip associated with the 1992 M_w 6.1 Joshua Tree, California, earthquake: implications for the Joshua Tree–Landers earthquake sequence, *J. Geophys. Res.* **100,** 6443–6461.

Bennett, R. A., W. Rodi, and R. E. Reilinger (1996). Global Positioning System constraints on fault slip rates in southern California and northern Baja, Mexico, *J. Geophys. Res.* **101,** 21,943–21,960.

Brown, R. D. (1990). Quaternary deformation, in *The San Andreas Fault System, California*, R. E. Wallace (Editor), *U.S. Geol. Surv. Profess. Pap. 1515*, 83–113.

Dorsey, R. J. (2003). Late Pleistocene slip rate on the Coachella Valley segment of the San Andreas fault and implications for regional slip partitioning, Presented at 99th Annual Meeting, Cordilleran Section, Geological Society of America, April 2003, Puerto Vallarta, Mexico.

Feigl, K. L., D. C. Agnew, Y. Bock, D. Dong, A. Donnellan, B. H. Hager, T. A. Herring, D. D. Jackson, T. H. Jordan, R. W. King, S. Larsen, K. M. Larson, M. M. Murray, Z.-K. Shen, and F. H. Webb (1993). Space geodetic measurements of crustal deformation in central and southern California, 1984–1992, *J. Geophys. Res.* **98,** 21,677–21,712.

Hartzell, S. H., and T. H. Heaton (1983). Inversion of strong ground motion and teleseismic waveform data for the fault rupture history of the 1979 Imperial Valley, California, earthquake, *Bull. Seism. Soc. Am.* **73,** 1553–1583.

Hauksson, E. (2000). Crustal structure and seismicity distribution adjacent to the Pacific and North America plate boundary in southern California, *J. Geophys. Res.* **105,** 13,875–13,903.

Hudnut, K. W., Y. Bock, J. E. Galetzka, F. H. Webb, and W. H. Young (2002). The Southern California Integrated GPS Network SCIGN, in *Seismotectonics in Convergent Plate Boundary*, Y. Fujinawa and A. Yoshida (Editors), Terrapub, Tokyo, 167–190.

Johnson, H. O. (1993). Techniques and studies in crustal deformation, *Ph.D. Thesis*, University of California, San Diego.

Johnson, H. O., D. C. Agnew, and F. K. Wyatt (1994). Present-day crustal deformation in southern California, *J. Geophys. Res.* **99,** 23,951–23,974.

Keller, E. A., M. S. Bonkowski, R. J. Korsh, and R. J. Shlemon (1982). Tectonic geomorphology of the San Andreas fault zone in the southern Indio Hills, Coachella Valley, California, *Geol. Soc. Am. Bull.* **93,** 46–56.

Kendrick, K. J., D. M. Morton, S. Wells, and R. W. Simpson (2002). Spatial and temporal deformation along the northern San Jacinto fault, southern California: implications for slip rates, *Bull. Seism. Soc. Am.* **92,** 2782–2802.

King, N. E., and J. C. Savage (1983). Strain-rate profile across the Elsinore, San Jacinto, and San Andreas faults near Palm Springs, California, 1973–81, *Geophys. Res. Lett.* **10,** 55–57.

King, R. W. (1997). Documentation for the GAMIT GPS Analysis Software, Department of Earth, Atmospheric, and Planetary Sciences, MIT.

Larsen, S., R. Reilinger, H. Neugebauer, and W. Strange (1992). Global Positioning System measurements of deformation associated with the 1987 Superstition Hills earthquake: evidence for conjugate faulting, *J. Geophys. Res.* **97,** 4885–4902.

Richards-Dinger, K. B., and P. M. Shearer (2000). Earthquakes in southern California obtained using source-specific station terms, *J. Geophys. Res.* **105,** 10,939–10,960.

Rockwell, T. K., C. C. Loughman, and P. M. Merrifield (1990). Late Quaternary rate of slip along the San Jacinto fault zone near Anza, southern California, *J. Geophys. Res.* **95,** 8593–8605.

Savage, J. C. (1995). Principal component analysis of interseismic deformation in southern California, *J. Geophys. Res.* **100,** 12,703–12,718.

Savage, J. C., and M. Lisowski (1995). Interseismic deformation along the San Andreas fault in southern California, *J. Geophys. Res.* **100,** 12,703–12,717.

Savage, J. C., and W. H. Prescott (1973). Precision of Geodolite distance measurements for determining fault movements, *J. Geophys. Res.* **78,** 6001–6008.

Savage, J. C., M. Lisowski, and W. H. Prescott (1996). Observed discrepancy between Geodolite and GPS distance measurements, *J. Geophys. Res.* **101,** 25,547–25,552.

Sieh, K. (1986). Slip rate across the San Andreas fault and prehistoric earthquakes at Indio, California, *EOS* **67,** 1200.

Sieh, K. E., and P. L. Williams (1990). Behavior of the southernmost San Andreas fault during the past 300 years, *J. Geophys. Res.* **95,** 6629–6645.

Wald, D. J., and T. H. Heaton (1994). Spatial and temporal distribution of slip for the 1992 Landers, California, earthquake, *Bull. Seism. Soc. Am.* **84,** 668–691.

Wessel, P., and W. H. F. Smith (1991). Free software helps map and display data, *EOS* **72,** 441, 445–446.

Wessel, P., and W. H. F. Smith (1998). New, improved version of Generic Mapping Tools released, *EOS* **79,** 579.

Appendix A

Disturbed Benchmarks

Two of the marks we reoccupied had changed significantly between the time of the last trilateration observation and our GPS surveys. BLUFF NO 1 1939 (bluff_rm1 for trilateration measurements; our code BLUF), the site used for trilateration measurements, was damaged. Our GPS observations were at the mark SDGPS 09 RM 1 (SD91) set by San Diego County in 1991 in an existing piece of concrete. We made GPS ties in 1997 between the original mark, BLFO, and the azimuth mark BLFA and between SD91 and its main mark, SD09. In 1995 the USGS made a GPS tie between BLFA and SD09. Combining all these, we get a horizontal distance of 28.444 m from BLFO to SD91 (total distance 28.477 m) in azimuth 10.79°. The National Geodetic Survey (NGS) taped distance from BLFO to BLUF was 28.466 m in azimuth 10.80°. SD91 was clearly set in the BLUF monument; field examination suggests that SD91 was in the same horizontal location as BLUF to within a few millimeters.

SODA was set in a 10-cm-diameter concrete-filled iron pipe that projected about 20 cm above the ground, which we found broken at ground level when we originally reoccupied the site in 1997; we therefore observed at SODA NO 2 1939 (SOD2). On 1997:252, we reset SODA's broken pipe to its original position and simultaneously observed at SODA and SOD2 to make an eccentric correction from SOD2 to SODA. We compared the original SODA–SOD2 horizontal distance and azimuth from the NGS datasheet for SODA to our GPS-derived values and found no significant difference, but given the residual dilatation for subnetworks involving SODA (seen in Fig. 8c), we may have small errors in our eccentric corrections due to uncorrected deformation of SODA's pipe.

Appendix B

Anomalous Motion of ALSA

None of our models fit at 95% confidence the combined trilateration/GPS data for the five baselines to ALSA (ALSA–COCG, ALSA–OBCH, ALSA–SALT, ALSA–SALV, and ALSA–SODA). Since none of the other measurements into COCG, OBCH, SALT, SALV, and SODA show any departure from steady motion, we believe that the explanation is movement of ALSA between 1987.95 and 1995.11.

If the north and east components of ALSA's anomalous displacement are Δ_N and Δ_E, then the change in length d_i of the ith baseline is

$$d_i = \Delta_N \cos(\alpha_i) + \Delta_E \sin(\alpha_i),\ i = 1, 2, \ldots, N, \quad \text{(B1)}$$

where α_i is the azimuth for baseline i. Using this equation and the observed offsets on the five ALSA baselines, we find a least-squares best-fit motion of ALSA of 35.6 ± 8.1 mm along an azimuth of 253.8° ± 9.5°; we show this motion and the individual baseline vector offsets in Figure B1a. Figure B1b shows the expected offset from equation B1 as a function of azimuth (solid line with 95% confidence limits), which matches the observed offsets (shown as circles) well, supporting our assumption that ALSA moved anomalously. Additionally, we compared GPS ties between ALSA and its three nearby reference marks (RMs) (see Table 1) to mea-

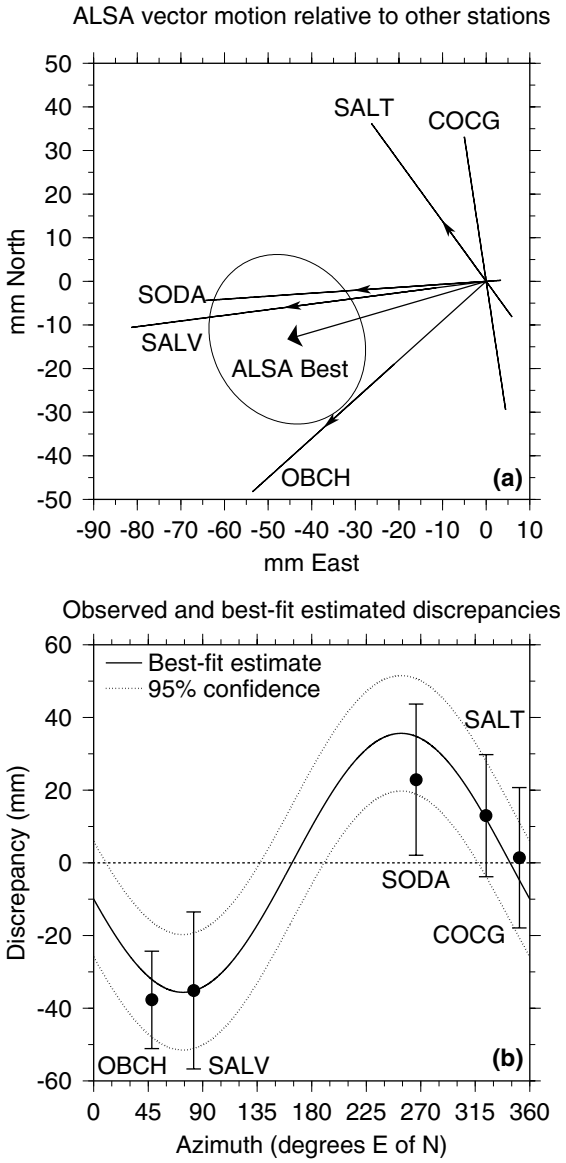

Figure B1. (a) Black vectors with thin arrowheads show the observed offsets in the ALSA baselines. Thin lines show 95% confidence limits on the observed offsets. Heavy arrow with wide head and 95% confidence limit shows best-fit motion of ALSA. (b) Solid line with dotted lines representing 95% confidence intervals shows baseline offsets expected due to ALSA best-fit motion. Circles with 95% confidence bars are observed offsets for Alamo baselines; these are fit well by the best-fit model.

surements made when the RMs were set, and we conclude that ALSA has remained stable (at $\leq$5 mm) relative to the RMs, indicating that a larger area than ALSA alone moved anomalously.

We believe this motion reflects deformation caused by nearby geothermal power production. Production at the Salton Sea geothermal field began in 1982, and in 1990 it was increased by a factor of 20; also, the production wells are located within 4 km of ALSA and to its south and southwest. The timing of production and expected direction of surface motion due to subsidence from it are consistent with ALSA's anomalous motion.

Cecil H. and Ida M. Green Institute of Geophysics and Planetary Physics
University of California, San Diego
La Jolla California 92093-0225

Manuscript received 8 January 2003.